

## Simulation of Performance Parameters of Mercury Cadmium Telluride Infrared Photodetectors

Hasan KOÇER<sup>1</sup> Yılmaz DURNA<sup>2</sup> Murat DEMİR<sup>3</sup>  
Önder Haluk TEKBAŞ<sup>4</sup>

### Abstract

In thermal imaging, HgCdTe (Mercury Cadmium Telluride) infrared (IR) photodetectors are widely used to sense IR radiation from targets. Their performance is strongly dependent on the material and device parameters of HgCdTe photodetectors. In this study, a developed numerical program (MCTsim or KOCERSim) is applied to investigate the electrical and photoelectrical properties of long-wave IR (LWIR) and very long-wave IR (VLWIR) p-on-n homojunction HgCdTe photodiodes at 77 K. KOCERSim solves nonlinear and coupled Poisson and continuity equations. Diffusion, radiative, Auger, Shockley-Read Hall (SRH) and trap-assisted tunneling (TAT) recombination-generation (R-G) mechanisms are well incorporated into KOCERSim solver. Effects of these R-G mechanisms on the dark and photocurrent are observed when applied reverse bias, cutoff wavelength, lifetime, capture-cross sections, trap density and trap energy level change.

**Keywords:** Simulation-based design, Infrared, photodetector, HgCdTe.

## Civa Kadmiyum Tellürüt Kızılötesi Foto Algılayıcıların Performans Parametrelerinin Simülasyonu

### Öz

Termal görüntüleme, HgCdTe (Civa Kadmiyum Tellürüt) kızılötesi foto algılayıcılar hedefin yansıttığı/yaydığı IR ışımının algılanması için yaygın olarak kullanılmaktadır. Bunların performansı/kalitesi kullanılan HgCdTe foto algılayıcının malzeme ve cihaz parametrelerine göre değişmektedir. Bu çalışmada, KOCERSim veya MCTsim adı verilen sayısal program geliştirilerek uzun dalga kızılötesi ışımaya (LWIR) ve çok uzun dalga kızılötesi ışımaya (VLWIR) bantlarındaki p-n tipi HgCdTe kızılötesi sensörün 77 K sıcaklıktaki elektriksel ve fotoelektriksel parametreleri incelenmektedir. KOCERSim programı doğrusal olmayan ve kuplajlı Poisson ve süreklilik denklemlerini çözmektedir. Difüzyon, ışımaya, Auger, Shockley-Read Hall (SRH) ve tuzak-destekli tünelleme (TAT) mekanizmaları KOCERSim programına uygun olarak eklenmiştir. Bu mekanizmaların karanlık ve fotoakıma olan etkileri ters öngerilimleme, kesim dalga boyu,

<sup>1</sup> Yazışma adresi: Dr.Müh.Bnb., Kara Harp Okulu Dekanlığı, Elektronik Mühendisliği Bölümü, Ankara, hkocer@kho.edu.tr.

<sup>2</sup> Y.Müh.Yzb. Kara Harp Okulu Dekanlığı, Elektronik Mühendisliği Bölümü, Ankara.

<sup>3</sup> Dr.Müh.Bnb., Kara Harp Okulu Dekanlığı, Elektronik Mühendisliği Bölümü, Ankara.

<sup>4</sup> Doç.Dr.Müh.Yb., NATO Daimi Delegasyonu Temsilcisi Bürüksel, Belçika.

elektron/hol yakalanma kesit alanı, ömür süresi, tuzak yoğunluğu ve tuzak enerji seviyesine göre incelenmektedir.

**Anahtar Kelimeler:** : Simülasyon tabanlı tasarım, kızılötesi, foto algılayıcı, HgCdTe.

## Introduction

Infrared (IR) region just starts where human eye stops seeing. Fig. 1 shows the IR spectral region in the electromagnetic spectrum. The first IR region is called Near IR (NIR) and Short Wave IR (SWIR). In this region, Night Vision Goggles (NVG) using image intensifier tubes ( $I^2T$ ) and some lasers (wavelength of  $1.064 \mu\text{m}$  and  $1.54 \mu\text{m}$ ) are operated. Imaging principles in the NIR and SWIR region are basically similar to visible region because both regions use reflected rays for detection. On the other hand, radiated IR rays are detected in mid-wave IR (MWIR), long-wave IR (LWIR), very long-wave IR (VLWIR) and far IR.

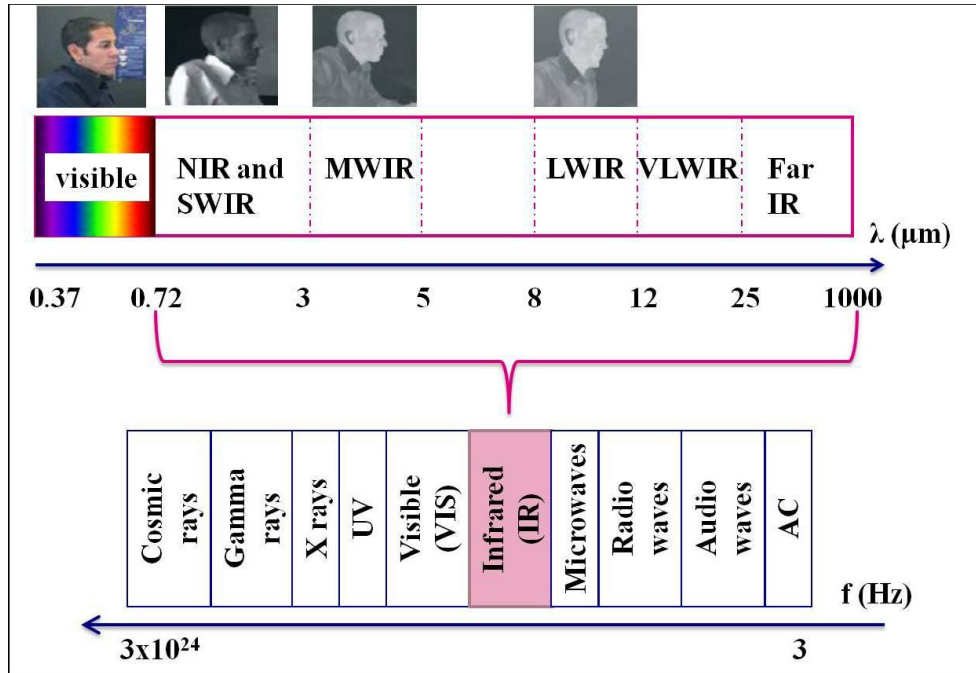


**Figure 1.** IR and Visible Ranges in Electromagnetic Spectrum (Koçer, 2011).

IR detectors (photodetector, photodiode, sensor or photovoltaic p-n diode) are widely used in military and civilian applications from thermal imaging of targets to the medical nondestructive imaging of the human body. The performance of an IR imaging system depends on target signature, environmental conditions, and building components of the imager. A basic block diagram of an IR imager is given in Fig. 2. The detector is the heart of the imaging system to sense IR radiation.

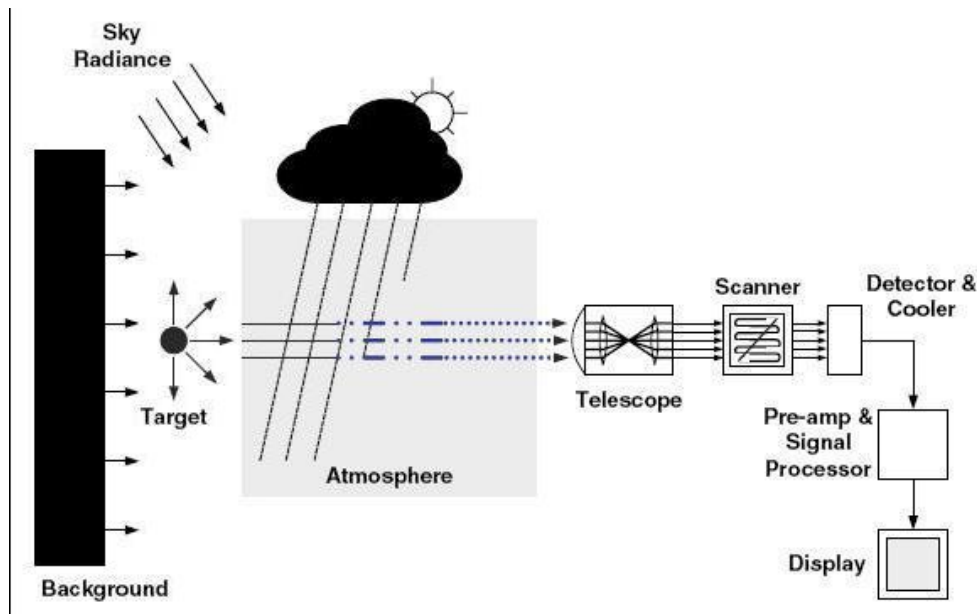


**Figure 2.** Block Diagram of an IR Imaging System (Koçer, 2011).

As seen in Fig. 3. (a), p-n diode type photodetector structures are generally used to detect IR radiation. When no IR radiation exists, current (I)-voltage (V) plot of the detector is called “dark” characteristics. When IR radiation exists, I-V plot is called “illuminated” characteristics. Difference of the currents under illumination and dark condition is the photocurrent as in Fig. 3. (b). Photodetectors are operated under reverse-bias condition. High photo and low dark currents are desired to increase the performance of the detector.

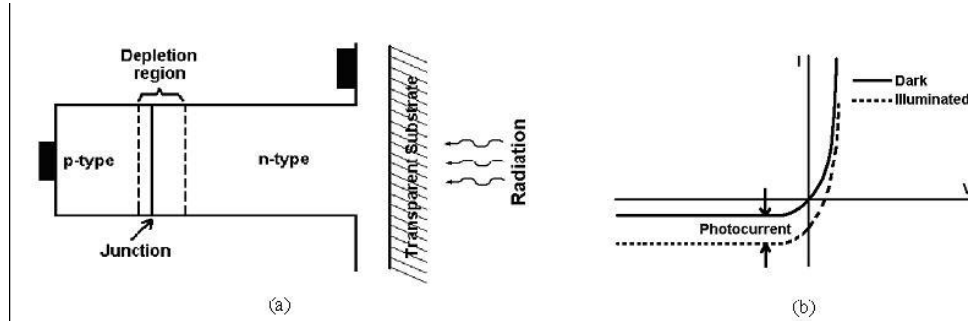


**Figure 3.** Geometry (a), and I-V curve (b) of a Photodetector (Koçer, 2011).

In IR spectrum, atmosphere is transparent to LWIR, MWIR and VLWIR. Therefore, low energy band-gap semiconductor photodetectors are used to sense these radiations. Most widely utilized semiconductors are HgCdTe (Mercury Cadmium Telluride-MCT), InSb (Indium Antimonide), InAsSb (Indium Arsenic Antimonide) and QWIP (Quantum Well Infrared Photodetector).  $\text{Hg}_{1-x}\text{Cd}_x\text{Te}$  is one of the most important semiconductors for IR detection.  $\text{Hg}_{1-x}\text{Cd}_x\text{Te}$  is produced with the alloy of HgTe and CdTe compounds. It is a direct bandgap material. Its absorption coefficient which provides high quantum efficiency, is very high.  $x$  represents CdTe mole fraction (i.e. percentage of CdTe) in the MCT alloy. Maximum detectible wavelength, which is called cutoff wavelength can be adjusted from 0.7 to 20  $\mu\text{m}$  by changing the CdTe mole fraction.

In order to improve the HgCdTe photodetector performance, its photoelectrical properties need to be deeply understood and optimized using successful numerical device simulators. In other words, dark current generating mechanisms and parameters should be deeply understood so that dark current should be decreased by controlling these parameters and detector performance should be increased. In HgCdTe diodes, various recombination-generation mechanisms affect the dark current. Generation is a process whereby electrons and holes are created. Conversely, recombination is a reverse process whereby electrons and holes are destroyed. Several recombination and generation (R-G) mechanisms occur in a semiconductor, each of which are modeled by different mathematical relations. In HgCdTe semiconductor, effective R-Gs are diffusion, Shockley-Read Hall (SRH), radiative, Auger and trap-assisted tunneling (TAT).

Simulation in engineering offers a powerful tool if we use it creatively and appropriately. Simulation-based design can provide an enormous amount of insight into how physical systems work. Setting up the simulation of a physical system and studying the results of the simulation is a useful way of deeply understanding and optimizing the system (Kramer, 1997).

Limited works have been realized in HgCdTe photodiode numerical device simulation. Most works used diffusion, SRH, radiative and Auger rates at 77K. Some works were at room temperature. Most of the studies used commercial device simulators like ATLAS and Sentaurus (Hu, 2008). Summers and Darling (1986) developed a numerical technique to solve the carrier transport equations for several homojunction HgCdTe photodiode configurations, namely  $n^+pp^+$ ,  $n^+np$  and  $pin$  at 77K in LWIR spectral region. Their work includes three important carrier recombination mechanisms that limit carrier lifetimes in HgCdTe: SRH, radiative and Auger recombination. But they did not use generation-recombination rate of TAT which is a very significant contributor to the dark current at low temperature and low band-gap photodetectors like HgCdTe. For total current noise of room temperature HgCdTe photodiodes, Karimi et al. (2007) included Johnson-Nyquist noise, generation-recombination noise, and dark current shot noise. In Saxena's recent study (Saxena, 2011), the performance of  $p^+-n-n^+$  HgCdTe LWIR homojunction photodetector ( $x \approx 0.22$ ) has been analyzed theoretically and simulated numerically using commercial ATLAS software from SILVACO. In this study, the author includes Johnson-Nyquist and shot noises in the calculation of detectivity. Although the author states that the current noise often increases under a reverse bias, due presumably  $1/f$  noise in the dark (leakage) current, the numerical model does not include  $1/f$  noise. Note that  $f$  in the  $1/f$  means frequency of the measurement.

HgCdTe infrared photodiodes are widely used to sense IR radiation from targets. Their performance is strongly dependent on the material and device parameters of HgCdTe photodiodes. In this study, a numerical solver is developed to simulate  $p^+n$  homojunction HgCdTe LWIR and VLWIR photodiodes. This solver serves a good numerical tool to deeply analyze and optimize photo-electrical behavior of LWIR and VLWIR HgCdTe IR photodiodes. In other words, dark and photo currents are evaluated more realistically to assess the performance with respect to certain device parameters. The solver computes nonlinear and coupled Poisson and continuity equations in one dimension. All important recombination-generation mechanisms including TAT are well incorporated into the code

to evaluate the performance of the HgCdTe device at 77K. Then, optimum device parameters are determined after solver runs at dark and illuminated conditions. Also, the solver isolates numerically dark current contributions of different recombination-generation mechanisms.

## Modeling Approach

### Figures of Merits for IR Photon Detectors

IR photon detectors are assessed according to certain figures of merit. These parameters are briefly discussed below (Koçer, 2011).

#### Responsivity

Responsivity is the change of detector output signal with respect to the incoming IR radiation (Karimi et al., 2007).

$$R_I = \frac{\text{Photocurrent (A)}}{\text{Photon Power (W)}} = \frac{I_{ph}}{P_{det}} \quad (1)$$

where  $P_{det}$  is the power of incoming IR radiation in Watt.

#### Noise

Noise is unwanted fluctuations at the detector output. There are several noise mechanisms for photodetectors such as thermal, generation-recombination (g-r) and 1/f noises given below (Niedziela and Ciupa, 2000).

$$i_{n-thermal}^2 = \frac{4kT\Delta fA}{R_d A} \quad (2)$$

$$i_{n-gr}^2 = 2q(I_{dark} + I_{ph})\Delta f = 2qI_{total}\Delta f \quad (3)$$

$$i_{n-1/f}^2 = \left[ \frac{\alpha I_{tot}^\beta}{f^{0.5}} \right]^2 \Delta f \quad (4)$$

where  $R_d = \left( \frac{\partial I}{\partial V} \right)^{-1}$  is detector's dynamic resistance,  $I_{dark}$  is dark current,  $I_{ph}$  is the photo current,  $k$  is Boltzmann constant,  $q$  is the electron charge,  $A$  is the area of the detector,  $T$  is the temperature,  $\Delta f$  is the measurement

bandwidth and  $f$  is the measurement frequency.  $\alpha=1 \times 10^{-6}$  ( $A^{0.5}$ ) and  $\beta=0.5$  are taken from Nemirovsky et al. (1992).

Total current expression is as follows

$$i_n = \sqrt{i_{n-thermal}^2 + i_{n-gr}^2 + i_{n-1/f}^2} \quad (5)$$

### **Specific Detectivity**

The detectivity is defined as the inverse of noise equivalent power (NEP), where NEP is the minimum amount of signal power in order to obtain unity signal-to-noise ratio. However, as the square of the noise current is directly proportional to the detector area and the measurement bandwidth, a sensitivity parameter which is independent from the detector area and measurement bandwidth should be defined, so called specific detectivity  $D^*$  expressed as (Niedziela and Ciupa, 2000)

$$D^* = \frac{R_l A \Delta f^{1/2}}{i_n} \quad (6)$$

where  $\Delta f$  is the measurement bandwidth and  $i_n$  is the total root-mean-square (rms) noise current. In our study, thermal, g-r and  $1/f$  noises were computed from numerical simulations according to noise current expressions.

### **Transport Equations**

Transport equations form the basis for the mathematical modeling of nonlinear current and voltages along the simulated HgCdTe device. In this study, drift-diffusion (DD) equations are solved in one dimensional space and steady-state conditions. In these conditions, coupled nonlinear DD equations that consist of Poisson and electron/hole continuity are as follows

$$\frac{d^2 V(x)}{dx^2} = -\frac{q}{\epsilon} C(x) + p(x) - n(x) \quad (7)$$

$$\frac{dJ_n(x)}{dx} = q R(x) - G(x) \quad (8)$$

$$\frac{dJ_p(x)}{dx} = -q R(x) - G(x) \quad (9)$$

where  $R(x)$ - $G(x)$  is the applicable recombination-generation mechanisms which will be detailed on the Section 2.4.  $C(x)$  is the net doping profile (positive ionized donor doping density plus negative ionized acceptor doping density along the device).  $n(x)$  and  $p(x)$  are the electron and hole concentrations.  $J_n(x)$  and  $J_p(x)$  are electron and hole current densities.  $\epsilon$  is the dielectric constant of the HgCdTe.

### MCTsim (KOCERSim) Numerical Solver

In our study, one dimensional Poisson and continuity equations form a boundary value problem (BVP) for investigation of HgCdTe photodiode. We use MATLAB language to solve numerically the coupled nonlinear Poisson and continuity equations. We have developed a numerical solver named as (MCTsim or KOCERSim). Its input-output parameters are shown in Fig. 4. The numerical method in the solver employs iterative finite-difference algorithm. Unknowns are  $n(x)$ ,  $p(x)$  and  $V(x)$ . Programme starts with an initial distribution of the unknowns subject to the ohmic condition boundary values at the contacts of the detector. Then, MCTsim converges to a stable solution. All output parameters and detector figures of merits can be computed using these unknowns. Hence, performance parameters of the detector can be extracted more realistically.

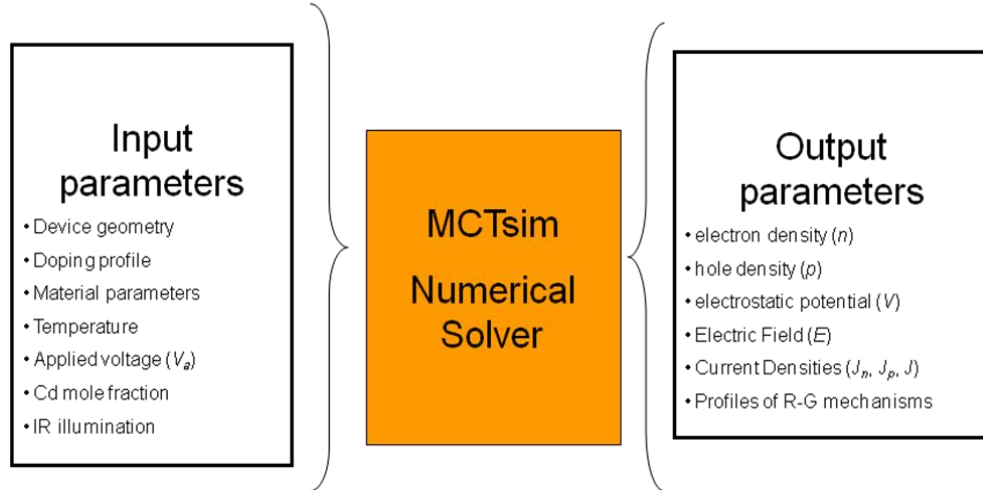


**Figure 4.** Input-Outputs of the MCTsim Programme.

### Recombination-Generation Mechanisms

In HgCdTe pn material, important recombination-generation processes include SRH, Auger, radiative, TAT and photogeneration. Description and mathematical modeling of these processes are introduced as follows. SRH recombination mechanism emerges from the recombination of electron-hole pairs via defect/impurity levels within the energy band-gap of the material. Therefore, SRH is not an intrinsic process. The excess energy is released via phonon (heat) emission. Such defect levels in MCT could be a result of vacancies, substitutional impurities, interstitial impurities, dislocations or grain boundaries. They can be generated during HgCdTe growth, post-growth annealing treatments or during device processing. The effect of this mechanism on the detector noise and the detectivity can therefore be decreased as HgCdTe growth and processing improve. However, considering state-of-the-art HgCdTe material and device processing, SRH is currently an essential recombination mechanism to take into account (Emelie, 2009). The net SRH recombination rate is given by (Summers and Darling, 1986)

$$R_{SRH}(x) = \frac{[n.p - n_i^2]}{[\tau_p n + n_1 + \tau_n p + p_1]} \quad (10)$$

where  $\tau_n$  and  $\tau_p$  are minority carrier lifetimes due only to SRH processes.

$$p_1 = N_v \exp -E_t / kT \quad (11)$$

$$n_1 = N_c \exp - E_g - E_t / kT \quad (12)$$

$n_1$  and  $p_1$  are the electron and the hole concentrations respectively when the Fermi level is coincident with the trap level. Trap level ( $E_t$ ) is the energy level of the traps in the HgCdTe. Its unit is eV.  $E_t$  is measured from the top of the valence band (Gumenjuk et al., 2001).  $N_c$  and  $N_v$  are the effective density of states in the conduction and valence bands respectively (Saxena and Chakrabarti, 2009).

$$N_c = 2 \left( \frac{3E_g kT}{8\pi P^2} \right)^{1.5} \left( 1 + 4kT / E_g \right) \quad (13)$$

$$N_v = 10^{-6} \left( \frac{2\pi m_{hh} kT}{4(\pi\hbar)^3} \right)^{1.5} \quad (14)$$

where  $m_{hh}$  is the heavy hole effective mass, which equals to  $0.55m_0$ .  $m_0$  is electron mass in vacuum. Interband transition matrix element,  $P=0.83$  eVnm (Gumenjuk and Sizov, 1999).

The theoretical study of radiative recombination has been developed by Shockley and Read (1952). In our study, the radiative and Auger recombination is modeled as follows (Summers and Darling, 1986)

$$R_{rad}(x) = G_R [n \cdot p - n_i^2] \quad (15)$$

$$R_{Aug}(x) = G_{Ae} \cdot n + G_{Ah} \cdot p \cdot [n \cdot p - n_i^2] \quad (16)$$

where  $G_R$ ,  $G_{Ae}$  and  $G_{Ah}$  are radiative, electron and hole Auger coefficients respectively and are described as follows (Bellotti and D'orsogna, 2006)

$$G_R = 5.8x10^{-13} \varepsilon_{r\_hf}^{1/2} \left( \frac{m_0}{m_e + m_{hh}} \right)^{3/2} \left( 1 + \frac{m_0}{m_e} + \frac{m_0}{m_{hh}} \right) \quad (17)$$

$$x \left( \frac{300}{T} \right) \left[ E_g^2 + 3kTE_g + 3.75k^2T^2 \right]$$

where  $m_0$ ,  $m_e$  and  $m_{hh}$  are free, electron and heavy hole effective masses.  $\varepsilon_{r\_hf}$  is high frequency dielectric coefficient.

$$G_{Ae} = \frac{\left( \frac{m_e}{m_0} \right) |F_1 F_2|^2}{2n_i^2 3.8x10^{-18} \varepsilon_{r\_hf}^2 \left( 1 + \frac{m_e}{m_{hh}} \right)^{\frac{1}{2}} \left( 1 + 2 \frac{m_e}{m_{hh}} \right)} \quad (18)$$

$$x \left( \frac{E_g}{kT} \right)^{-\frac{3}{2}} e^{\left[ \frac{1+2 \frac{m_e}{m_{hh}} E_g}{1 + \frac{m_e}{m_{hh}} kT} \right]}$$

$$G_{Ah} = G_{Ac} \left[ \frac{1 - \frac{3E_g}{kT}}{6 \left( 1 - \frac{5E_g}{4kT} \right)} \right] \quad (19)$$

where  $|F_1 F_2|$  is the overlap integral and is in the range 0.1-0.3. In our study, we assume that  $|F_1 F_2| = 0.2$  (Bellotti and D'orsogna, 2006).

TAT is the dominant dark current mechanism under large and moderately large reverse bias voltages (Rosenfeld and Bahir, 1992). Therefore, modeling the TAT rate is extremely important for HgCdTe IR photodiodes. In literature, limited work has been performed for sophisticated mathematical modeling of TAT rate, which can be embedded into the continuity equations for numerical analysis (Rogalski, 1995). Examining these works, we adopt following expressions for TAT rate (Gumenjuk et al., 2001)

$$R_2 = N_t n_i^2 \left[ n \cdot p - n_i^2 \right] \left[ W_v \cdot W_c \cdot e^{E_g/kT} + W_c \cdot \gamma_v \cdot e^{(E_g - E_t)/kT} + W_v \cdot \gamma_c \cdot e^{E_t/kT} + \gamma_c \cdot \gamma_v \right] \quad (20)$$

$$R_3 = p + p_1 \cdot \gamma_v + n + n_1 \cdot \gamma_c + \left[ n \cdot e^{(E_g - E_t)/kT} + N_c \right] \cdot W_c + \left[ p_{lh} \cdot e^{E_t/kT} + N_{vlh} \right] \cdot W_v \quad (21)$$

$$R_{TAT} = \frac{R_2}{R_3} \quad (22)$$

where  $N_{vlh}$  is the density of states of light holes in the valence band which is taken approximately equal to  $N_c$  (Gumenjuk and Sizov, 1999).  $N_t$  is trap density.  $p$  is the sum of the densities of the light ( $p_{lh}$ ) and heavy holes. Light holes are responsible for tunneling since mass of light hole is small and tunneling rate is large. In our study,  $p_{lh} \approx (N_{vlh}/N_{vhh})p$ . Electron and hole tunnel capture constants are given as follows (Nemirovsky et al., 1991).

$$W_c = \frac{6 \times 10^5 E_{max}}{N_c (E_g - E_t)} \cdot \exp \left[ \frac{-1.7 \times 10^7 E_g^{1/2} (E_g - E_t)^{3/2}}{E_{max}} \right] \quad (23)$$

$$W_v = \frac{6 \times 10^5 E_{max}}{E_t} \cdot \exp \left[ \frac{-1.7 \times 10^7 E_g^{1/2} \cdot E_t^{3/2}}{E_{max}} \right] \quad (24)$$

Electron and hole thermal capture constants are given as follows (Gumenjuk and Sizov, 1999)

$$\gamma_c = \frac{1}{\tau_n N_t} \quad (25)$$

$$\gamma_v = \frac{1}{\tau_p N_t} \quad (26)$$

The photogeneration rate is given by (Summers and Darling, 1986)

$$G_f(x) = F_f \alpha \eta e^{-\alpha x} \quad (27)$$

where  $\eta$  is the quantum efficiency,  $F_f$  is incident photon flux and  $\alpha$  is the absorption coefficient, which is in the range of 1000-2000  $\text{cm}^{-1}$  for HgCdTe (Rogalski et al., 2000). We chose Hougen formula for absorption coefficient given by (Hougen, 1989)

$$\alpha = 100 + 5000x \quad (28)$$

where  $x$  is Cd mole fraction.

### Device Structure and Material Parameters

Device under study is  $p^+$ -on- $n$  homojunction photodiode. IR flux is given from  $n$ -side which is active or absorber layer.  $n$ ,  $p^+$  side dopings and length of the  $p^+$  side are fixed at  $10^{15} \text{ cm}^{-3}$ ,  $10^{17} \text{ cm}^{-3}$ . and 2  $\mu\text{m}$  respectively.

Energy-bandgap and intrinsic carrier density expressions are taken from the literature (D'orsogna, 2010). Static dielectric constant in Poisson equation and the high frequency one in radiative and Auger rate expressions are obtained from previous studies (Mao, 1998; Emelie, 2009). Theoretical expressions of the mobility for  $T > 50\text{K}$  are used (Rosbeck et al., 1982). Electron and hole mobilities in HgCdTe are scaled based on the experimental data by keeping the electron to hole mobility ratio fixed at 166.5 (Mao, 1998). Electron effective mass is presented by (Emelie, 2009)

$$m_e = \frac{m_0}{-0.6 + 6.333 \left( \frac{2}{E_g} + \frac{1}{E_g + 1} \right)} \quad (29)$$

Cutoff wavelength is computed by (Jozwikowski et al., 2010)

$$\lambda_c (\mu m) = \frac{1.24}{E_g (eV)} \quad (30)$$

Minority carrier lifetime is an important parameter in the HgCdTe device modeling and simulation. In our study, lifetime is incorporated in SRH and TAT R-G expressions. Electron and hole lifetimes are modeled as follows (Ivasiv et al., 1999)

$$\tau_n = \frac{1}{\sigma_n v_{th,e} N_t} \quad (31)$$

$$\tau_p = \frac{1}{\sigma_p v_{th,p} N_t} \quad (32)$$

where  $v_{th}$  is electron/hole thermal velocity (cm/s).  $\sigma_n$  and  $\sigma_p$  are electron and hole capture cross-sections (cm<sup>2</sup>).

Deep levels may be related to the impurities, dislocations and defects during the fabrication of the p-n junction. In the literature, there is very limited deep level transient spectroscopy (DLTS) data for p on n detector in HgCdTe ( $x \approx 0.2$ ) (Polla and Jones, 1981; Yoshino et al., 1998). Most works have been focused on extraction of these trap parameters by analytical fitting on the experimental data (Gopal et al., 2002, Razeghi, 2002, Hu et al., 2008). In our study, we examine effects of varying trap parameters on the performance of HgCdTe photodiode by numerical method. Measured capture cross sections are ranged from  $10^{-18}$  to  $10^{-11}$  cm<sup>2</sup> (Polla and Jones, 1981). We fix both electron and hole capture cross sections to  $10^{-16}$  cm<sup>2</sup>, and change  $E_t$  and  $N_t$  in the numerical simulations given on the next section.

## Results And Discussion

In this part, results of several numerical simulations have been presented for the analysis of following aspects of p on n HgCdTe homojunction IR photodiode:

- Effect of absorbing layer thickness on the performance,
- At the optimal device layer thickness, behavior of dark/photocurrents and performance parameters ( $R_dA$ , current responsivity, noise and specific detectivity) in LWIR and VLWIR spectra with the sweep of the reverse bias,
- At the cutoff wavelength and bias of the maximum specific detectivity, behavior of the performance parameters with respect to the trap density and the trap energy level.

**Table 1.** Simulation Parameters.

Parameter	Value
Pixel area	25 $\mu\text{m}$ x 25 $\mu\text{m}$ =6.25x10 <sup>-6</sup> cm <sup>2</sup>
$d_{abs}$	8 $\mu\text{m}$
$N_d$ (donor doping)	10 <sup>15</sup> cm <sup>-3</sup>
$N_a$ (acceptor doping)	10 <sup>17</sup> cm <sup>-3</sup>
$T$	77 K
$N_t$	10 <sup>14</sup> cm <sup>-3</sup>
$E_t$	0.5E <sub>g</sub>
$\sigma_n, \sigma_p$	10 <sup>-16</sup> cm <sup>2</sup>
electron lifetime	1.63 $\mu\text{s}$ @ $N_t=10^{14}$ cm <sup>-3</sup>
hole lifetime	12.5 $\mu\text{s}$ @ $N_t=10^{14}$ cm <sup>-3</sup>
$\mu_n$ (electron mobility)	50,000 cm <sup>2</sup> /(V.s) @ $\lambda_c=10$ $\mu\text{m}$ and $T=77\text{K}$
$\mu_p$ (hole mobility)	300 cm <sup>2</sup> /(V.s) @ $\lambda_c=10$ $\mu\text{m}$ and $T=77\text{K}$
$L_n$	232.8 $\mu\text{m}$ @ $\lambda_c=10$ $\mu\text{m}$ and $T=77\text{K}$
$L_p$	50 $\mu\text{m}$ @ $\lambda_c=10$ $\mu\text{m}$ and $T=77\text{K}$
$n_i$	5.34x10 <sup>12</sup> cm <sup>-3</sup> @ $\lambda_c=10$ $\mu\text{m}$ and $T=77\text{K}$
$\alpha$	1230 cm <sup>-1</sup> @ $\lambda_c=10$ $\mu\text{m}$
$f/\#$	2
Background Temp.	300 K
$\Delta f$	1 Hz
$f$	1 kHz

Baseline simulation parameters are given in Table 1. Effective R-G mechanisms are radiative, Auger, SRH, TAT and photogeneration.

In our analysis, all current components (such as TAT, dark, dark without TAT, photocurrent, dark without Auger mechanism) are computed by considering interactions of all these effective R-G mechanisms. For that purpose, a practical method is implemented to numerically extract these currents. In this method, desired R-G mechanism is purposely enabled and disabled in the continuity equation part of the solver. Then, difference in the output currents of the two consecutive numerical simulations gives us the contribution of that mechanism to the current output.

#### Effect of $d_{abs}$

In this part, we have examined the active layer thickness on the performance. Device structure is simulated with Table-1 parameters at 77 K,  $V_a = -0.1V$ , 10  $\mu m$  cut-off and variable  $d_{abs}$  values in the range of 2 to 20  $\mu m$ . As seen in Fig. 5, dark current is increased as the absorbing layer decreases because pn diode behaves like a narrow diode according to Eq. 33.

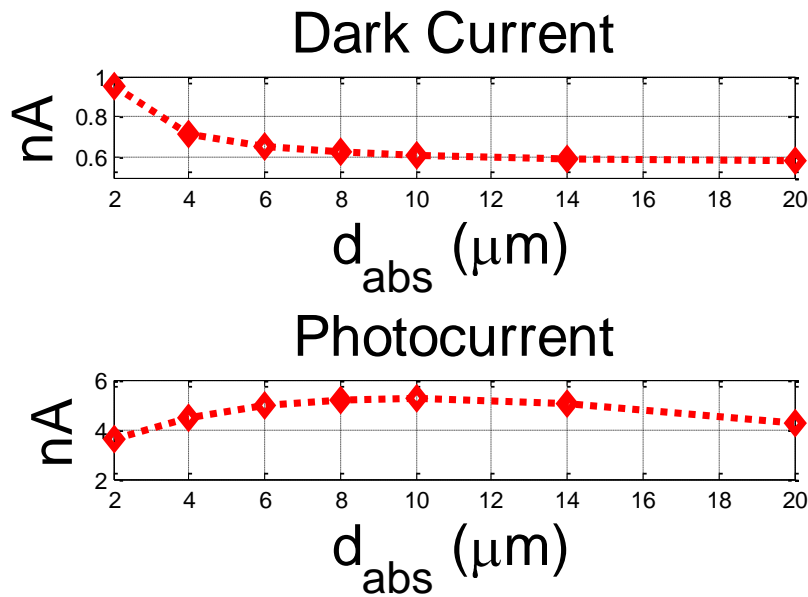


**Figure 5.** Dark and Photocurrents With Applied Bias When  $d_{abs}$  is Variable.

Photocurrent is maximized at absorbing layer of 10  $\mu m$  which is compatible with the experimental (Nemirovsky and Unikovsky, 1992) and simulation (Niedziela and Ciupa, 2000, Karimi et al., 2007) results. Note that similar simulation formulas are used in those studies.

$$I_o = qA \left( \frac{D_p p_n}{W_p} + \frac{D_n n_p}{W_n} \right) \quad (33)$$

where  $I_o$  is analytical dark current expression,  $D_{p,n}$  are the hole/electron diffusivities,  $A$  is the detector area, and  $W_{p,n}$  are the widths of neutral p and n layers. In our case, hole diffusion length ( $L_p$ ) is 50  $\mu\text{m}$ , which is greater than the  $d_{abs}$ . This condition satisfies the requirement of the narrow diode. In order to achieve high detection parameters of photodiode, total absorption of radiation inside the active region of photodiode must occur and conditions of low thermal generations of carriers must be created (Niedziela and Ciupa, 2000). In other words, Eq. 34 must be fulfilled for optimal performance. Here,  $1/\alpha$  is the penetration depth of the IR radiation inside the HgCdTe photodiode. Our absorption coefficient ( $\alpha$ ) in this simulation is  $1230 \text{ cm}^{-1}$ . So, penetration depth ( $1/\alpha$ ) is 8.13  $\mu\text{m}$ .

$$\frac{1}{\alpha} \ll d_{abs} \ll L_p \quad (34)$$

We observe this photonic characteristic apparently in our numerical photocurrent result of Fig. 5. When  $d_{abs} < 10 \mu\text{m}$ , photocurrent monotonously increases with the increase of  $d_{abs}$ . Here, the photo absorption is the dominant mechanism. After  $d_{abs}$  is equal and just greater than the penetration depth, photocurrent saturates then eventually decreases with further increase of the  $d_{abs}$ .

As shown in Fig. 6, we obtain current responsivity to be 2.342 A/W at absorbing layer of 10  $\mu\text{m}$ . This value of current responsivity well agrees with the previous optimization studies of HgCdTe photodiode (Niedziela and Ciupa, 2000), where similar simulation formulas are used.

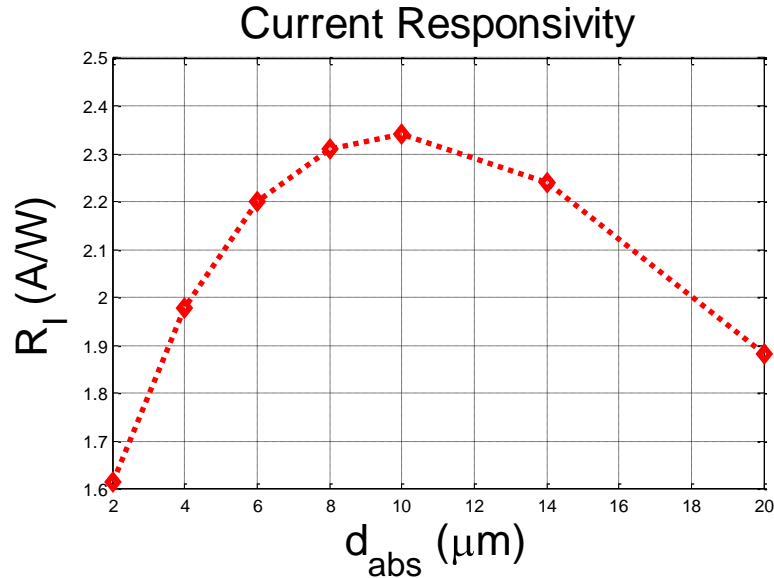


**Figure 6.** Current responsivity when  $d_{abs}$  is variable.

### **Behavior of current components and performance in LWIR and VLWIR spectral regions**

In this simulation, photodiode structure has been analyzed with  $d_{abs}=8 \mu\text{m}$  which has been optimized to have maximal current responsivity. Cutoff wavelength (or Cd mole fraction) is swept from 9 to 14  $\mu\text{m}$  with 1  $\mu\text{m}$  steps. Cut-in wavelength is kept constant to be 8  $\mu\text{m}$ . Also, applied reverse bias is swept in the range of -0.4 V to -5 mV. Numerically extracted current components are exhibited in Fig. 7. Using these data, further analyses were implemented as shown in Figs. 8 to 12. Fig. 8 exhibits that increasing speed (or magnitude of the gradient) of the TAT % becomes slower. This strange behavior can be explained such that as the cutoff and reverse bias increases, not only  $I_{tat}$  increases but also  $I_{dark}$  does because  $I_{dark}$  already includes  $I_{tat}$ , but its dominancy appears at reverse biases larger than -0.2 Volt.

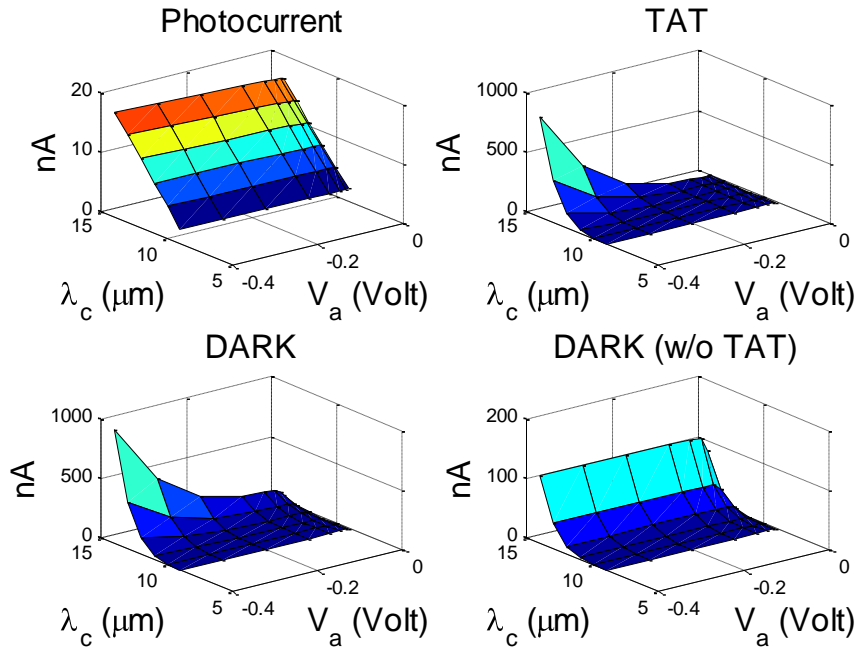


**Figure 7.** Photocurrent, Dark, TAT and Dark Without TAT Currents with Respect to Cutoff Wavelength ( $\lambda_c$ ) and Applied Bias ( $V_a$ ) Voltage.

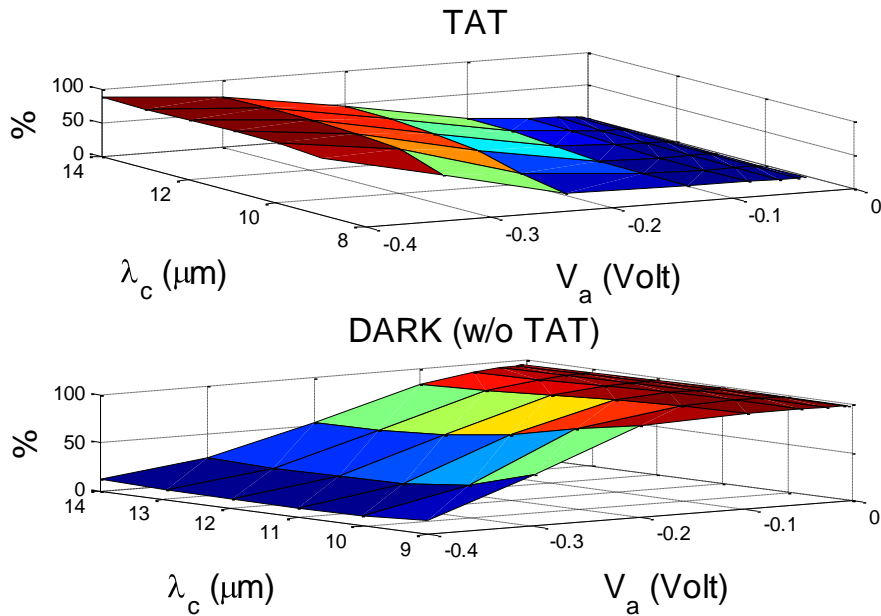


**Figure 8.** Percentages of TAT and Dark Without TAT Currents with Respect to Cutoff Wavelength ( $\lambda_c$ ) and Applied Bias ( $V_a$ ) Voltage.

$R_dA$  (Dynamic resistance-area product) is shown in Fig. 9. We see that  $R_dA$  decreases at large reverse bias due to TAT and at close to zero bias due to diffusion, radiative and Auger rates. At cutoff wavelength of 9  $\mu\text{m}$  and reverse bias of -0.1 V, it reaches maximum value of  $3.664 \times 10^5 \Omega \cdot \text{cm}^2$  in the simulation conditions. At  $\lambda_c = 10 \mu\text{m}$  and  $V_a = -25 \text{ mV}$ , we obtain  $R_dA = 759.1 \Omega \cdot \text{cm}^2$  which is the order of the experimental observations (Gopal et al., 2002). If we approach to  $V_a = -10 \text{ mV}$  at the same cutoff wavelength, we reach a reduced value of  $R_dA = 203.2 \Omega \cdot \text{cm}^2$  since diffusion and other intrinsic recombination processes (radiative, Auger) start to dominate. For LWIR p+-n HgCdTe diodes at 77 K, experimental  $R_dA$  at zero bias ( $R_{dA}$ ) is around 100-200  $\Omega \cdot \text{cm}^2$  (Gopal et al., 2002). Our numerical  $R_dA$  is compatible with the experiment (Joswikovski et al., 2010) showing the accuracy and reliability of our numerical modeling and simulation.

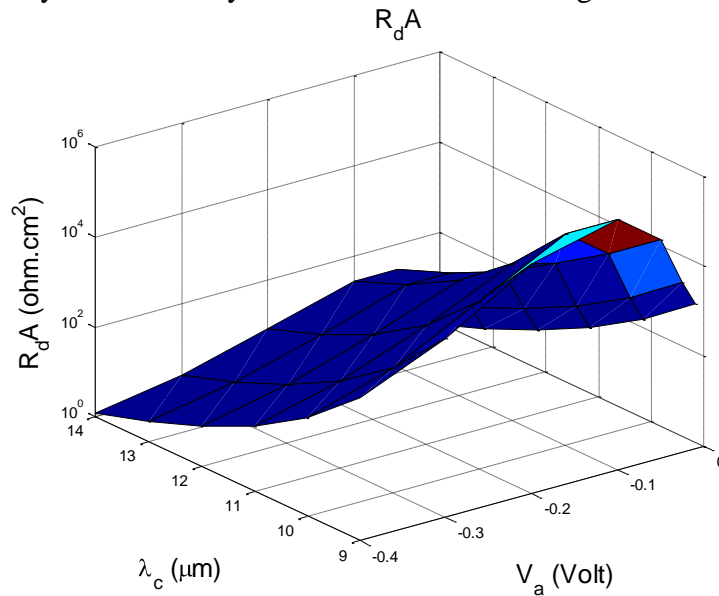


**Figure 9.**  $R_dA$  with Respect to Cutoff Wavelength ( $\lambda_c$ ) and Applied Bias ( $V_a$ ) Voltage.

In Fig. 10, current responsivity, which is computed as photocurrent divided by IR flux intensity ( $H$  in  $\text{W}/\text{cm}^2$ ), is observed to be maximized towards the VLWIR region.

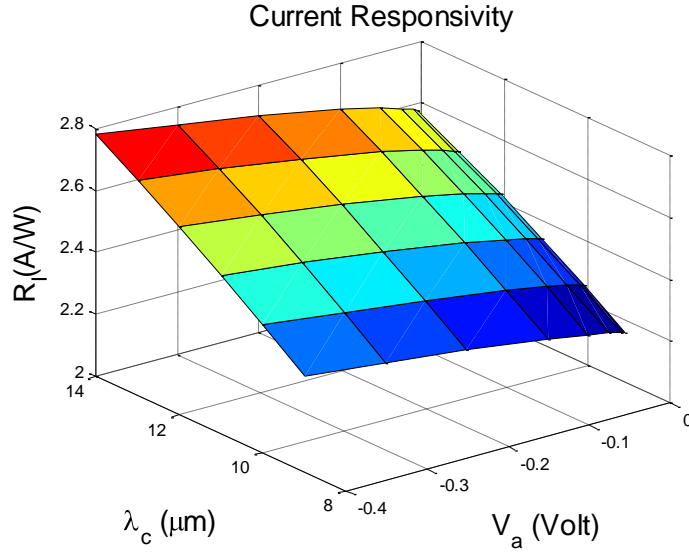


**Figure 10.** Current responsivity with respect to cutoff wavelength ( $\lambda_c$ ) and applied bias ( $V_a$ ) voltage.

As seen in Fig. 11, maximum  $D^*$  of  $1.915 \times 10^{11} \text{ cm.Hz}^{1/2}/\text{W}$  was obtained at  $9 \mu\text{m}$  cutoff and slight reverse bias of  $-10 \text{ mV}$  in our simulation conditions.  $D^* = 1.125 \times 10^{11} \text{ cm.Hz}^{1/2}/\text{W}$  at the same bias and  $10 \mu\text{m}$  cutoff. As cutoff wavelength and the magnitude of the reverse bias increase,  $D^*$  decreases due to the increase in the total noise current as observed in Fig. 12. With our simulation parameters and the wavelength/bias range, we have found that minimum  $D^*$  of  $2.388 \times 10^8 \text{ cm.Hz}^{1/2}/\text{W}$  occurs at  $14 \mu\text{m}$  cutoff and  $-0.4 \text{ V}$  bias.

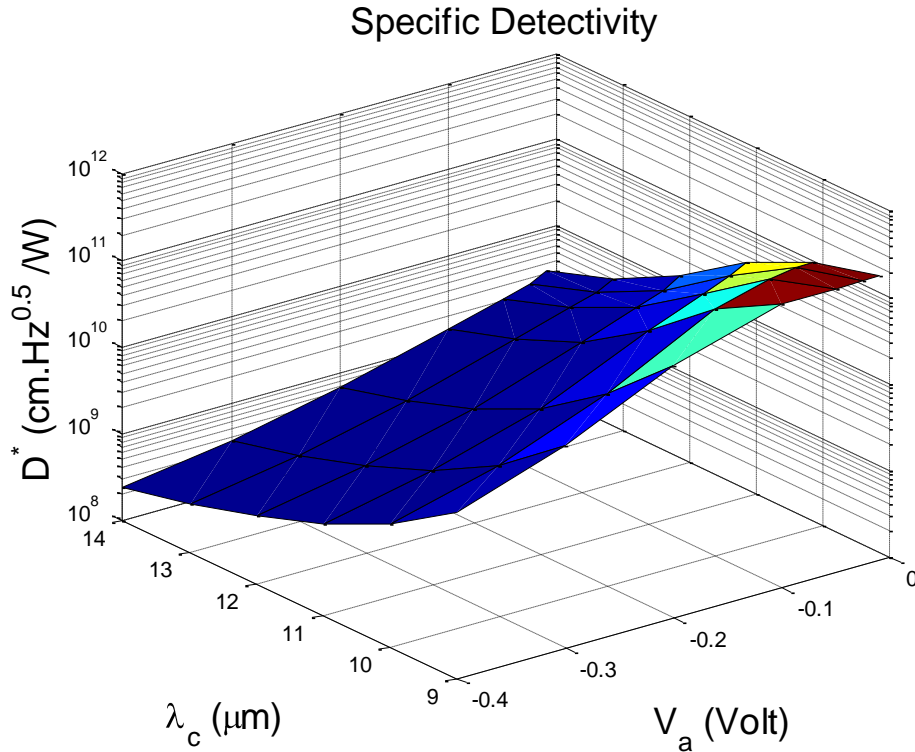


**Figure 11.** Specific detectivity ( $D^*$ ) with respect to cutoff wavelength ( $\lambda_c$ ) and applied bias ( $V_a$ ) voltage.

We observe from Fig. 12, at  $\lambda_c=14 \mu\text{m}$  and bias=-0.4 V, thermal, g-r, 1/f and total noise currents are found to be  $1.47 \times 10^{-13}$ ,  $5.594 \times 10^{-13}$ ,  $2.909 \times 10^{-11}$  and  $2.909 \times 10^{-11}$  A/Hz<sup>0.5</sup> respectively. We see here that 1/f noise is the dominant one at these conditions. On the other hand, at  $\lambda_c=10 \mu\text{m}$  and bias=-10 mV, thermal, g-r, 1/f and total noise currents are found to be  $1.144 \times 10^{-14}$ ,  $4.223 \times 10^{-14}$ ,  $1.499 \times 10^{-14}$  and  $4.624 \times 10^{-14}$  A/Hz<sup>0.5</sup> respectively and our results are in reasonable agreement with the measurement of HgCdTe photodiodes (Nemirovsky and Unikovski, 1992) confirming the validity of our modeling and simulation approach. We extract from Fig. 12 that 1/f noise is the main contributor to the noise current as the cutoff increases in the reverse bias. It depends on TAT current which are monitored numerically in Figs. 7 and 8. Therefore, through numerical simulations, we see more deliberately that efforts to reduce TAT process has a positive impact on the HgCdTe photodiode performance in terms of the noise current and the specific detectivity. Another observation of Fig. 12 is related to thermal noise reduction around -0.1 V. This is caused by the

maximization of the dynamic resistance-area product behavior as shown in Fig. 9.

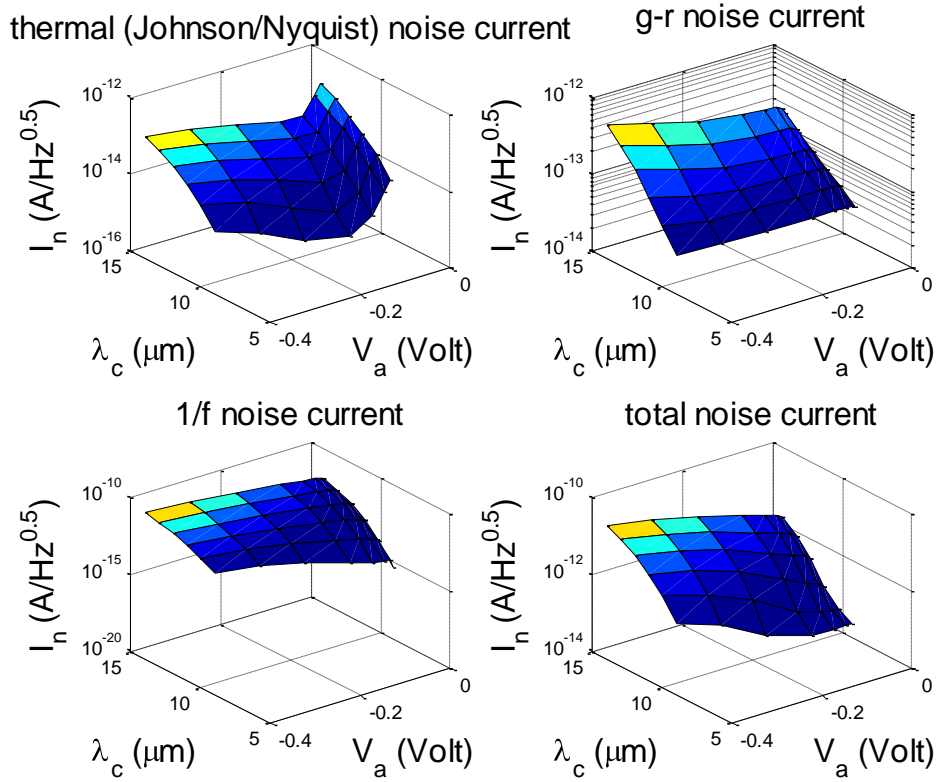


**Figure 12.** Total and Components of Noise Currents with Respect to Cutoff Wavelength ( $\lambda_c$ ) and Applied Bias ( $V_a$ ) Voltage.

### From Theory to Practice

Our theoretical observations in the simulations can be used in designing real HgCdTe IR photodetectors for thermal imaging. Performance of the practical IR sensors are expected to be maximized and/or optimized under the guidance of the following simulation results:

- In order to obtain best photocurrent performance of the real photodetectors, absorbing layer thickness of the real HgCdTe LWIR photodiode should be adjusted around  $10 \mu\text{m}$ .

- LWIR HgCdTe photodetectors are shown to have better performance compared to VLWIR since degrading effect of the TAT is observed to increase in the VLWIR region.
- Real VLWIR photodetector performance can be improved if TAT current can be decreased. Therefore, it seems that exceptionally trap-free material is practically required to achieve desirable imaging performance in the VLWIR band.

## Conclusion

In thermal imaging, HgCdTe IR photodetectors are widely used to sense IR radiation from targets. Their performance is strongly dependent on the material and device parameters of HgCdTe photodetectors.

In this study, p<sup>+</sup>n homojunction HgCdTe photodiode performance has been analyzed with the help of a comprehensive numerical simulation in the LWIR and VLWIR spectral regions. All important recombination-generation mechanisms including TAT are well incorporated into the numerical solver to evaluate performance of the HgCdTe device at 77K. Dark and IR illuminated simulations were performed.

Real HgCdTe photodetectors are used in various military and civil thermal imaging systems where they operate under IR illuminated conditions. In our study, numerically obtained currents were extracted by considering the IR illumination effect. In LWIR and VLWIR spectra, we have determined that photocurrent increases with the cutoff wavelength and dark current becomes dominated as the cutoff wavelength and applied reverse voltage increase due to the fact that contribution of TAT increases as the band gap decreases and the electric field increases. On the other hand, magnitude of the gradient of the TAT % becomes slower. Reason for this strange behavior was explained with the help of numerically extracted TAT and dark current ratios. At cutoff wavelength of 9  $\mu\text{m}$  and reverse bias of -0.1 V, we have obtained the maximum value of  $R_dA$  to be  $3.664 \times 10^5 \Omega \cdot \text{cm}^2$ . At  $\lambda_c = 10 \mu\text{m}$  and  $V_a = -25 \text{ mV}$ , we obtained  $R_dA = 759.1 \Omega \cdot \text{cm}^2$ . If we approach to  $V_a = -10 \text{ mV}$  at the same cutoff wavelength, we obtain a reduced value of  $R_dA = 203.2 \Omega \cdot \text{cm}^2$  since diffusion and other intrinsic recombination processes (radiative, Auger) starts to dominate.

Results of this study can be used as a guide for optimization of the performance of HgCdTe detectors with various cutoff wavelengths in the LWIR and VLWIR bands for thermal imaging purposes.

## References

- Bellotti, E. ve D'orsogna, D. (2006). Numerical Analysis of HgCdTe Simultaneous Two-Color Photovoltaic Infrared Detectors, *IEEE Journal of Quantum Electronics*, 42(4), 418-426.
- D'orsogna, D. (2010). Numerical Simulation Models and Stress Measurements for HgCdTe Infrared Detectors HgCdTe, BostonUniversity, PhD Thesis.
- Emelie, P.Y. (2009). HgCdTe Auger-Suppressed Infrared Detectors Under Non-Equilibrium Operation, The University of Michigan, PhD Thesis.
- Gumenjuk, J.V., Sizov F.F., Ovsiuk V.N., Vasil'ev V.V. ve Esaev D.G., (2001). Charge Transport in HgCdTe-Based n+-p Photodiodes, *Semiconductors*, 35(7), 835-840.
- Gumenjuk, J.V. ve Sizov F.F. (1999). Currents in Narrow-Gap Photodiodes, *Semiconductor Science and Technology*, 14, 1124-1131.
- Gopal, V., Singh S.K. ve Mehra R.M. (2002). Analysis of Dark Current Contributions in Mercury Cadmium Telluride Junction Diodes, *Infrared Physics & Technology*, 43, 317-326.
- Hougen, C.A. (1989). Model for Infrared Absorption and Transmission of Liquid-Phase Epitaxy HgCdTe, *Journal of Applied Physics*, 66, 3763-3767.
- Hu, W. D., Chen X. S., Yin F., Ye Z.H., Lin C., Hu X. N., Quan Z. J., Li Z. F. ve Lu W. (2008). Simulation and Design Considerations of Photoresponse for HgCdTe Infrared Photodiodes, *Optical and Quantum Electronics*, 40, 1255-1260.
- Ivasiv, Z. F., Sizov F.F. ve Tetyorkin V.V. (1999). Noise Spectra and Dark Current Investigations in n+-p-type Hg<sub>1-x</sub>Cd<sub>x</sub>Te (x≈0.22) Photodiodes, *Semiconductor Physics, Quantum Electronics & Optoelectronics*, 2(3), 21-25.
- Jozwikowski, K., Kopytko M., Rogalski A. and Jozwikowska A. (2010). Enhanced Numerical Analysis of Current-voltage Characteristics of Long Wavelength n-on-p HgCdTe Photodiodes, *Journal of Applied Physics*, 108, 074519-1-074519-11.

- Karimi, M., Kalafi M. and Asgari A. (2007). Numerical Optimization of an Extracted HgCdTe IR Photodiodes for 10.6-um Spectral Region Operating at Room Temperature, *Microelectronics Journal*, 38, 216-221.
- Koçer, H. (2011). Numerical Modeling and Optimization of HgCdTe Infrared Photodetectors for Thermal Imaging, METU, Ph.D. Thesis.
- Kramer, K. (1997). *Semiconductor Devices: A Simulation Approach*. New Jersey/US: Prentice Hall PTR.
- Mao, D. H. (1998). Optical and Electrical Characterization of Mercury Cadmium Telluride and Performance Simulation of Infrared Photodetectors, Stanford University, PhD Thesis.
- Nemirovsky, Y., Fastow R., Meyassed M. and Unikovsky A. (1991). Trapping Effects in HgCdTe, *Journal of Vacuum Science and Technology*, B9(3), 1829-1839.
- Nemirovsky, Y. and Unikovsky A. (1992). Tunneling and 1/f Noise in HgCdTe Photodiodes, *Journal of Vacuum Science and Technology B*, 10(4), 1602-1610.
- Niedziela, T. and Ciupa R. (2000). Optimization of Parameters of (Hg,Cd)Te n+-p Photodiodes for 10.6-um Spectral Region Operating at Near-Room Temperatures, *Electron Technology*, 33(4), 542-547.
- Polla, D.L. and Jones C.E. (1981). Deep Level Studies of Hg<sub>1-x</sub>Cd<sub>x</sub>Te. I: Narrow-Band-Gap Space-Charge Spectroscopy, *Journal of Applied Physics*, 52(8), 5118-5131.
- Razeghi, M. (2002). *Handbook of Infrared Detection Technologies*. Washington/US: SPIE.
- Rogalski, A. (1995). *Infrared Photon Detectors*. Washington/US: SPIE.
- Rogalski, A., Adamiec K. and Rutkowski J. (2000). *Narrow-Gap Semiconductor Photodiodes*. Washington/US: SPIE Press.
- Rosenfeld, D. and Bahir G. (1992). A Model for The Trap-Assisted Tunneling Mechanism in Diffused n-p and Implanted n+-p HgCdTe Photodiodes, *IEEE Transactions on Electron Devices*, 39(7), 1638-1645.
- Rosbeck, J.P., Star R.E., Price S.L. and Riley K.J. (1982). Background and Temperature Dependent Current-Voltage Characteristics of HgCdTe Photodiodes, *Journal of Applied Physics*, 53, 6430-6440.
- Saxena, P.K. (2011). Modeling and Simulation of HgCdTe Based p+-n-n+ LWIR Photodetector, *Infrared Physics & Technology*, 38, 216-221.
- Saxena, P.K. and Chakrabarti P. (2009). Computer Modeling of MWIR Single Heterojunction Photodetector Based on Mercury Cadmium Telluride, *Infrared Physics & Technology*, 52, 196-203.

- 
- Shockley, W. and Read W. T. (1952). Statistics of The Recombinations of Holes and Electrons, *Physical Review*, 87, 835-842.
- Summers, C. J. and Darling B. (1986). Computer Modeling of Carrier Transport in (Hg,Cd)Te Photodiodes, *Journal of Applied Physics*, 59(7), 2457-2466.